Phase separation and surface segregation in Co – Au – SrTiO3 thin films: Self-assembly of bilayered epitaxial nanocolumnar composites

M. Hennes, X. Weng, E. Fonda, B. Gallas, G. Patriarche, D. Demaille, Y. Zheng, F. Vidal

Phase separation and surface segregation in Co-Au-$SrTiO_3$ thin films: self-assembly of bilayered epitaxial nanocolumnar composites

M. Hennes,[1] X. Weng,[1] E. Fonda,[2] B. Gallas,[1] G. Patriarche,[3] D. Demaille,[1] Y. Zheng,[1] and F. Vidal[1]

[1] *Sorbonne Université, CNRS-UMR 7588, Institut des NanoSciences de Paris, INSP, F-75005 Paris, France*
[2] *Synchrotron Soleil, L'Orme des Merisiers Saint-Aubin BP 48, 91192 Gif-sur-Yvette Cedex, France*
[3] *Centre de Nanosciences et de Nanotechnologies, CNRS / Université Paris Sud, Université Paris Saclay, Avenue de la Vauve, 91120 Palaiseau*

(Dated: February 14, 2019)

Phase separation and surface segregation are powerful levers that allow to synthesize nanocomposites via self-assembly. In the present work, we combine these concepts with 3-dimensional vertical epitaxial growth and study Co-Au-$SrTiO_3$ thin films as a model system. We demonstrate that $SrTiO_3$, Co and Au undergo phase separation during sequential pulsed laser deposition, giving rise to a dense array of ultrathin bilayered Co-Au nanowires (NWs) with highly anisotropic optical *and* magnetic properties. A detailed analysis of the structural properties of the embedded metallic NWs reveals stabilization of a Co fcc phase and pronounced coupling to the matrix, which leads to large magnetoelastic effects. We discuss possible growth mechanisms yielding bilayer phase separation in nanocolumnar composites and show how the present results can be used to estimate a lower bound for the Co/Au interface energy.

I. INTRODUCTION

Co-Au is an archetypal bimetallic system exhibiting very low bulk miscibility. The propensity of Co-Au mixtures to display pronounced phase separation effects has been known for decades [1] and theoretical work eventually confirmed that, at equilibrium, Co-Au nanoalloys composed of only several hundred atoms remain immiscible [2]. Thus, even in ultrasmall nanostructures, segregation can be used as an effective lever to grow hybrid systems consisting of combined Co-rich and Au-rich phases, which is especially interesting for future magnetoplasmonic applications [3–5]. To achieve full control over plasmonic and magnetic functionalities, not only the chemical composition, but also the shape and crystallographic orientation need to be adjusted in a precise way. However, the simultaneous tuning of these parameters in assemblies of ultrasmall immiscible nanoalloys has remained elusive so far. Phase segregated Co-Au nanostructures reported in literature are generally spherical [6–8]. In contrast, nanostructures obtained by filling nanopores display shape anisotropy but usually exhibit poor crystallinity [9]. In recent years, a novel approach based on nanoscale self-organization of metallic nanostructures embedded in various single-crystal oxide systems has been established, which allows to bridge the gap between epitaxy and shape tuning. Nanocolumnar composites consisting of elemental Fe, Ni, Co, Au, Pt, Ir nanowires epitaxied in different matrices such as $SrTiO_3$, $BaTiO_3$, $BaZrO_3$, or CeO_2 were successfully grown [10–16]. While the synthesis of nanowires consisting of miscible metals was also demonstrated [17, 18], results on systems with formation of more than two phases are scarce. In such hybrid thin films, judicious choice of the components can, in principle, give rise to a variety of nanoarchitectures, as depicted in Fig.1 (a-c). Self-assembled core-shell (CS) structures, with two oxide and a metallic phase, were recently reported [19]. In this paper, we focus on the combination of immiscible metals in an oxide matrix. Using Co-Au-$SrTiO_3$ (Co-Au-STO) as a three phase system, we show that the metallic nanocolumns exhibit a bilayer structure and display highly anisotropic magnetic and optical properties.

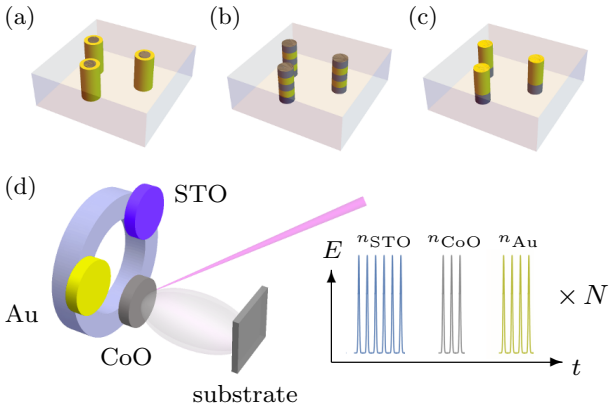

FIG. 1. Nanowires exhibiting (a) core-shell (CS), (b) multi- and (c) bilayer segregation patterns. (d) Schematics of sequential PLD.

II. EXPERIMENTS

For sample synthesis, we employed a sequential pulsed laser deposition (PLD) approach using a quadrupled Nd:YAG laser ($\lambda = 266\,\mathrm{nm}$, $\nu = 10\,\mathrm{Hz}$) and a fluence in the 1-3 $\mathrm{J/cm^2}$ range. Co-Au-STO metal-oxide thin films were deposited on $SrTiO_3(001)$ substrates ($T \simeq 650°\mathrm{C}$, $p_{\mathrm{base}} < 2 \cdot 10^{-9}\,\mathrm{mbar}$, $p_{\mathrm{growth}} < 5 \cdot 10^{-7}\,\mathrm{mbar}$). The growth sequences consisted of N repetitions of one basic sequence of n_{STO}, n_{CoO}, n_{Au} laser pulses on STO, CoO

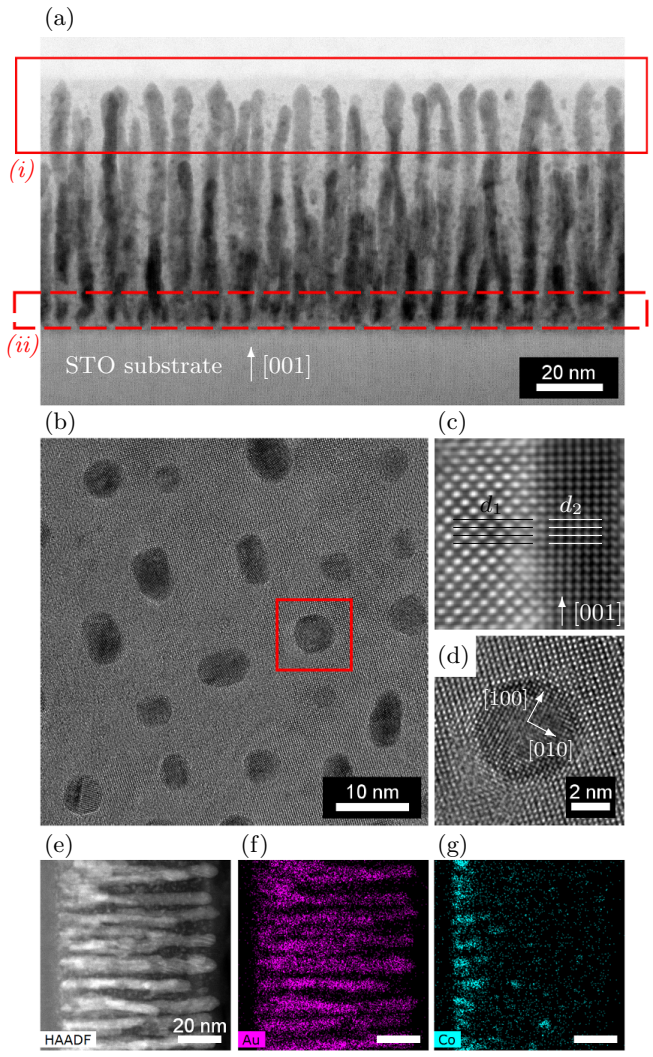

FIG. 2. Electron microscopy images of Co-Au-STO composite thin films. (a) Cross-sectional and (b) plan view. (c) HR-TEM imaging of the nanowire-STO interface in cross-sectional geometry (4.39 nm × 4.39 nm) and (d) single nanowire in plan view. (e-g) STEM-HAADF and EDX chemical mapping of Co and Au in cross-sectional view.

and Au targets respectively (Fig.1d). One Au-STO (S0) and three different Co-Au-STO samples (S1-S3) with increasing Co content were synthesized by increasing the ratio of ablation pulses $n_{\mathrm{Co}}/n_{\mathrm{Au}}$ on the CoO and Au targets, while keeping $n_{\mathrm{Co}} + n_{\mathrm{Au}}$ and n_{STO} constant. Each basic sequence deposited about 4 Å of equivalent Co-Au-STO nanocomposite thin film thickness.

The structure of the samples was studied using transmission electron microscopy (TEM), scanning transmission electron microscopy (STEM) in combination with a high-angle annular dark-field detector (HAADF), x-ray diffraction (XRD) and x-ray absorption spectroscopy (XAS). High resolution transmission electron microscopy (HRTEM) data were acquired using a JEOL JEM 2100F. STEM data were acquired using a Titan Themis 200. Energy-dispersive x-ray (EDX) spectroscopy was used to map chemical distributions. XRD data were collected on a laboratory diffractometer (Rigaku SmartLab) with Cu K_{α_1} radiation (λ = 1.54 Å). X-ray absorption spectroscopy data were gathered at the beamline SAMBA (Synchrotron SOLEIL) in fluorescence mode, with a beam incidence angle of 45° with respect to the sample surface. Magnetic properties were studied with vibrating sample magnetometry (VSM) using a Physical Property Measurement System (Quantum Design), while the optical response of the thin films was analysed via ellipsometry measurements (J. A. Woollam).

III. RESULTS

A. Structural analysis

1. *Nanoarchitecture and chemical composition*

Figure 2(a) shows a cross-sectional view of sample S1 with overall Co concentration $c_{\mathrm{Co}} = 10$ at%. The nanocomposite exhibits a columnar structure, with a dense scaffold of wires which extends from the bottom of the thin film to its surface. The nanowires show slight diameter variations, which can be ascribed to laser power fluctuations during growth. The seemingly higher density of wires at the bottom of the thin film is an artifact which results from the wedge-like shape of the TEM sample. A plan view of the same sample is given in Fig. 2(b). From such micrographs, the average diameters $\langle d \rangle$ of the wires were calculated and found close to 4 nm, slightly decreasing in size with increasing Co content.

TEM measurements were also used to provide information on the epitaxial relationship between the matrix and the embedded wires. Figure 2(c) shows the vertical interface between a nanowire and the STO matrix in vicinity of the thin film surface, unveiling excellent structural compatibility between the two phases ($d_1/d_2 \simeq 1$). Similar matrix and nanowire lattice parameters also become apparent in plane, as shown in Fig. 2(d), where cube-on-cube epitaxy is readily evidenced. In contrast to cross-sectional views, plan views only provide information about the upper 20 nm–25 nm of the thin film (Fig.2(a)*(i)*). The data reveal that the nanowire lattice parameter deduced from Fourier analysis a = 4.1Å is very close to pure bulk Au ($a^{\mathrm{Au}}_{\mathrm{bulk}}$=4.078 Å). The reason for complete absence of Co signature becomes apparent when performing a chemical mapping of the thin film in cross-sectional geometry. As shown in Fig. 2(e-g), the upper part of the wires consists exclusively of an Au-rich phase. In contrast, Co accumulates at the substrate interface. Some isolated Co-rich spots were evidenced within the thin film, which can be explained by STO overgrowth of a wire segment. While EDX mapping also indicates a significant amount of Au counts at the substrate-thin film interface (*e.g.* Fig.2(a)*(ii)* in sample

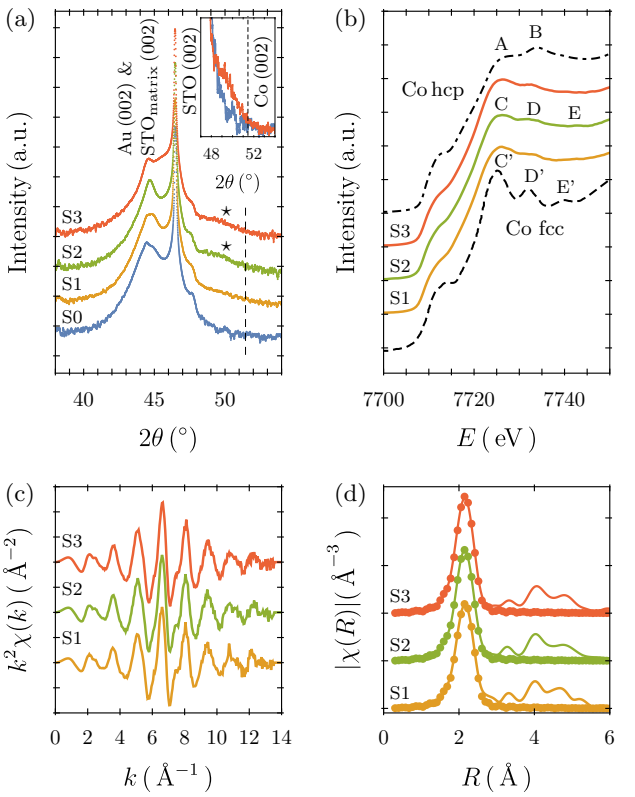

FIG. 3. Structural analysis of Co-Au-STO nanocomposites. (a) XRD θ-2θ in vicinity of the 002 substrate peak, (b) XANES spectra of samples S1-S3 and fcc-Co (dashed) and hcp-Co (dash-dotted) reference spectra. (c) k^2-weighted $\chi(k)$ data for samples S1-S3, and (d) $\chi(r)$ obtained after Fourier transformation (solid line), with fits to the nearest neighbor shell (dots).

S1), this cannot be attributed to Co-Au intermixing, as will become apparent in a later section.

2. *Crystallographic properties*

To complement our structural analysis of the thin films, the crystallographic properties of the latter were studied via XRD. Figure 3(a) shows θ-2θ measurements performed on samples S0-S3. Matrix, substrate and nanowire peaks can be identified, confirming the epitaxial nature of the composite growth. Superposition of STO(002) matrix and Au(002) diffraction peaks agrees with TEM data presented in Fig.2(c), hinting again at the excellent structural compatibility of Au and STO in out-of-plane direction. In fact, our PLD grown STO matrix exhibits a tetragonal distortion of several percent. This can be traced back to lattice defects and STO non-stoichiometry [20] and has been observed before in STO-based nanocolumnar composites [21, 22]. Finally, two small broad peaks can be identified at $2\theta = 49.7°$ in samples S2 and S3, which we attribute to a Co-rich fcc phase. As shown in Fig.3(a), their position is shifted, when compared to bulk Co, corresponding to a 3.3% increase of the lattice parameter ($a^{\mathrm{Co}}_{\mathrm{bulk}} = 3.548$Å). This axial strain is a consequence of strong interfacial coupling between the Co-phase and the surrounding oxide matrix[18, 21, 22].

Final evidence for full phase separation and stabilization of a Co fcc phase is eventually provided by XAS measurements. Figure 3(b) shows the x-ray absorption near edge (XANES) part of the averaged Co K-edge spectra obtained on samples S1-S3, as well as a Co foil reference spectrum measured in transmission mode. Background corrections and normalization were performed using the ATHENA (IFEFFIT) software [23]. All nanocomposite spectra exhibit very similar near edge features and can hardly be discerned. Comparison of the latter with data gained on the Co foil reveal poor agreement. While the characteristic hcp edge structure consists of two peaks, labeled A and B in Fig. 3(b), three different maxima (C, D and E) can be seen in the composite Co spectra. Their intensity decreases with increasing energy and their average separation equals 6.7±0.4 eV and 8.8±1.2 eV, respectively. This compares well [24] with Co fcc full multiple scattering calculations [25]. Indeed, the same decreasing peak intensity is found with increasing photon energy, and typical peak spacings are equal to 6.5 eV and 8.1 eV, respectively (C', D' and E'). The pronounced total intensity reduction and blurring of the Co-Au composite spectra can be ascribed to finite size and disorder effects [22]. For further quantification of our analysis, the extended absorption fine structure (EXAFS) of the spectra was analyzed as well. Figure 3(c) shows k^2-weighted $\chi(k)$ EXAFS spectra of samples S1-S3. Again, no fundamental difference between the data can be identified, another strong hint at complete phase separation in this system. Quantitative information was eventually extracted by fitting the nearest neighbor shell. Standard procedures using the ARTEMIS (IFEFFIT) software were employed [23]. In a first step, the amplitude reduction factor S_0^2 was determined by fitting the Co reference data, using a fixed value $N = 12$, while R, σ^2 and ΔE_0 were left floating. In a second step, the composites were modeled by using $S_0^2 = 0.76$, obtained from the reference fit, while using N, R, σ^2 and ΔE_0 as free parameters. The results of our *ansatz*, where we assume that Co atoms find themselves exclusively surrounded by Co neighbors in the first coordination shell, are given in Table 1. Small N values can again be ascribed to finite size effects and an increased atomic disorder, as reflected by the increased values of σ^2, when compared to the Co foil. The nearest neighbor distances however agree perfectly well with bulk data. The excellent match between the fit and the experimental EXAFS data allows to conclude that, in the present system, the immiscibility of Au and Co is bulk-like.

TABLE I. EDX data and Co K-edge EXAFS fit parameters.

Sample	c_{Co} (at%)	N	R (Å)	σ^2 (10^{-3}Å^2)
S1	10	6.9 ± 0.6	2.497 ± 0.006	7.9 ± 0.9
S2	24	7.7 ± 0.6	2.489 ± 0.005	8.4 ± 0.8
S3	53	7.6 ± 0.5	2.489 ± 0.006	7.9 ± 0.8
Co foil	100	12	2.492 ± 0.002	6.3 ± 0.3

B. Anisotropic magnetic and optical properties

Having evidenced the formation of vertically aligned phase separated CoAu nanowires, we now turn to an analysis of their magnetic and optical response. The optical properties of the composite thin films were determined from spectroscopic ellipsometry measurements ($400\,\mathrm{nm} < \lambda < 2500\,\mathrm{nm}$) for 3 angles of incidence (50°, 60° and 70°). The optical constants were extracted using a multilayer model using thicknesses and volume fractions determined by TEM measurements. The substrate had the tabulated optical constants of STO. The part of the film containing the Co wires was modeled with uniaxial optical anisotropy obtained using the Bruggeman effective medium approximation mixing the optical constants of Co and STO. The wires were modeled as elongated ellipsoids by modifying the depolarization factor according to the aspect ratio of the Co section of the wires. The effective optical constants of the part of the film containing the Au section of the wires were first determined wavelength by wavelength using an isotropic approximation to fit to all measurements simultaneously. Figure 4(a) presents the effective imaginary part of the dielectric constant, ϵ'', of the film containing the Au wires. Two absorption bands can be observed and could be attributed to the transverse and longitudinal plasmon resonances of the Au wires, labeled T and L, respectively. To confirm this, the ordinary and extraordinary optical constants of a film containing Au wires in STO were modeled using the Maxwell-Garnett effective medium approximation with depolarization factors according to the aspect ratio of the Au wires [26]. The optical conductivity of Au was damped to take into account the confinement effects and scattering at the Au/STO and Au/Co interfaces. Figure 4(a) presents these modeled optical constants together with the effective one. A very good agreement is observed in both positions and amplitudes of the absorption bands associated with the T and L plasmon resonances for the two approximations. This confirms that the Au wires support localized surface plasmon resonances.

Finally, Fig. 4(b) shows $M(H)$ data recorded in in-plane and out-of-plane geometry on sample S3. Close to zero in-plane coercivity and a large anisotropy field underpin the strong magnetic anisotropy of the system. An effective uniaxial anisotropy constant K_{eff} was estimated from temperature dependent measurements of coercive fields $H_c(T)$ (inset of Fig.4(b)) using $H_c = H_{c0}\left(1 - (25k_BT/E_b)^{2/3}\right)$, where E_b is the energy barrier for magnetization reversal [27]. $K_{\mathrm{eff}} = 4.4 \cdot 10^5\,\mathrm{J/m^3}$ is eventually obtained *via* $K_{\mathrm{eff}} = \frac{1}{2}\mu_0 M_s H_{c0}$, where M_s is the saturation magnetization of Co. A detailed interpretation of this result will be given in the last section of this paper.

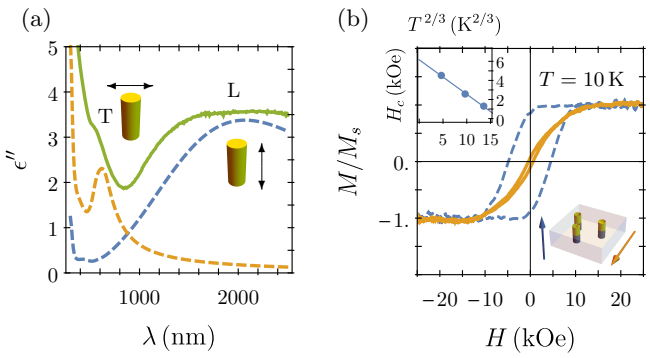

FIG. 4. (a) Imaginary part of the effective dielectric constant, ϵ'' of the layer containing Au wires in sample S3, determined by ellipsometry (solid line) and model ordinary and extraordinary ϵ'' for a STO film with oriented Au wires (dashed lines). (b) Magnetic hysteresis cycles in in-plane (solid line) and out-of-plane (dashed line) geometry obtained by VSM. Inset: fitted T-dependence of the coercive field.

IV. DISCUSSION

A. Growth mechanisms and phase separation

To identify the key mechanisms governing self-organization in three phase composites, it is helpful to recall earlier theoretical work on self-assembly of nanocolumnar thin films[16, 28]. During high temperature sequential PLD growth of metal-oxide composites, metal atoms deposited at the surface diffuse and aggregate into clusters which eventually evolve into thermodynamically stable islands. Meanwhile, the space inbetween these metallic structures is progressivly overgrown by the oxide matrix phase. Stacking of islands in consecutive steps gives rise to rods and nanowires, whose diameter and density will depend on the synthesis parameters like temperature, concentration and deposition rate[16]. It is important to stress that, in order to achieve a thorough description of the synthesis process, even in monometallic systems, vertical diffusion steps (in a direction perpendicular to the thin film surface) have to be explicitely taken into account[16]. This vertical mobility is a key ingredient required to understand the synthesis of immiscible multiphase systems. In fact, one striking feature of the present composite is that, despite depositing monolayer amounts of Co and Au in each step of

the sequential growth process, the wires finally adopt a bilayer segregation pattern. This indicates that two different phase separation phenomena are at work: in-plane segregation resulting in phase separation of $SrTiO_3$ and Co-Au on the one hand and demixing of Co and Au in the nanowires on the other hand. Complete segregation of Co and Au requires a high mobility of these two species inside the nanowire. An analysis of bulk diffusion coefficients reveals that typical diffusion lengths exceed the thin film thickness h ($64\,\mathrm{nm} < h < 80\,\mathrm{nm}$ for the samples S0-S3) by roughly two orders of magnitude. In contrast to other nanoalloy synthesis techniques, e.g., gas-phase-based growth[29], the present high temperature approach ensures that the bimetallic Co-Au wires do not get trapped into chemically mixed metastable states.

Providing a reliable prediction of segregation patterns in the present system remains a challenging task though. While great progress has been made in the field of nanoalloys[30, 31], most recent studies remained limited to freestanding bimetallic nanoparticles and nanowires[32–38]. Very little work is available on the segregation of metallic species in the presence of metal-oxide interfaces[39]. Here, instead of providing an atomic scale description of the segregation process, we propose a continuum model-based analysis relying on the competition of surface and interface energies. We will show that it can be used as a qualitative tool to rule out specific segregation patterns and, that it can be combined with the present experimental results to approximate the Co/Au interface energy.

B. Segregation patterns and interface energies

We start by comparing the bi- and multilayered structures, depicted in Fig.1(b-c). For both configurations, the topmost layer is expected to be Au-rich, which results from the large difference in surface energies between the two metals [40]. However, due to the poor compatibility between Co and Au, the creation of multiple Co/Au interfaces will lead to a strong increase in free energy of the system. Both configurations displaying identical Co/STO and Au/STO interface areas, this immediately provides a qualitative explanation for the absence of multilayer patterns in our experiments. We highlight that these considerations hint at a general problem affecting the synthesis of vertically aligned nanocomposites with multilayer geometry. Indeed, even when using appropriate sequential deposition schemes, the pronounced vertical mobility will be a serious issue that can hardly be overcome, considering the high growth temperatures required to induce in-plane metal-oxide phase separation.

In a similar fashion, the free energy of bilayer structures can be compared to that of their core-shell counterparts. Again, we only take the Co/Au, Co/STO and Au/STO interface energies $\gamma_{\mathrm{Co/Au}}$, $\gamma_{\mathrm{Co/STO}}$, $\gamma_{\mathrm{Au/STO}}$ into account and do not consider strain or atomic details at the interfaces. The wires are cylindrical with total height h and radius r. The CS configurations are characterized by an inner radius r_i, the bilayered wires consist of Au and Co segments with length h_{Au} and h_{Co}, respectively. For simplification, we neglect in-plane contributions to the overall free energy of the system ($r/h \ll 1$) and introduce the dimensionless parameter $R_\gamma = \frac{\gamma_{\mathrm{Au/STO}} - \gamma_{\mathrm{Co/STO}}}{\gamma_{\mathrm{Co/Au}}}$. The condition $E_{\mathrm{bilayer}} < E_{\mathrm{Au\,core-Co\,shell}}$, relating the energies of the two different segregation patterns, can be rewritten as $2\pi r(h_{\mathrm{Au}}\gamma_{\mathrm{Au/STO}} + h_{\mathrm{Co}}\gamma_{\mathrm{Co/STO}}) < 2\pi(rh\gamma_{\mathrm{Co/STO}} + r_i h\gamma_{\mathrm{Co/Au}})$. This is readily transformed into $\frac{\gamma_{\mathrm{Au/STO}} - \gamma_{\mathrm{Co/STO}}}{\gamma_{\mathrm{Co/Au}}} < \frac{r}{r_i} = (\alpha\frac{c_{\mathrm{Co}}}{c_{\mathrm{Au}}} + 1)^{1/2}$. Here α represents the volume ratio of elementary Co and Au fcc unit cells. In our experiments, even for very low Co concentrations, we exclusively observe bilayer configurations ($R_\gamma \lesssim 1$). Based on this observation, we can derive a lower bound for the Co/Au interface energy required to impede formation of Co-Au CS structures.

We first give a brief overview over available literature results required for our calculations. Data gained on fcc Co nanocrystals epitaxially grown on STO(001) (2×2) reconstructed surfaces yields a work of adhesion[41] $W_{\mathrm{Co/STO}} = 3.96 \pm 0.37\,\mathrm{J/m^2}$. This can be compared with *ab-initio* calculations performed on Co/STO/Co magnetic tunnel junctions with fcc-Co sandwiched between STO(001) layers (with TiO_2 termination and Co atoms placed in top O positions) where $W_{\mathrm{Co/STO}} = 3.39\,\mathrm{J/m^2}$ was derived[42]. For the Au/STO interface, DFT calculations yield an interface energy $\gamma_{\mathrm{Au/STO}} = 1.95\,\mathrm{J/m^2}$ for defect-free interfaces[43] while experimental work on vapor phase grown Au nanocrystals on $SrTiO_3$(001) (2×1) substrates revealed creation of Au(111)/STO(001) interfaces with[44] $\gamma_{\mathrm{Au/STO}} = 2.05 \pm 0.51\mathrm{J/m^2}$

With these data, two different approaches can be used to calculate $\gamma_{\mathrm{Au/STO}} - \gamma_{\mathrm{Co/STO}}$. First, we stick exclusively to the experimental work by Silly *et al.* where $\gamma^* = \gamma - E^{\mathrm{surf}}_{\mathrm{STO}}$ values were deduced through a straightforward analysis of the Au and Co nanocrystal geometry via a modified Wulff construction. From this, $\gamma_{\mathrm{Au/STO}} - \gamma_{\mathrm{Co/STO}}$ is calculated using $\Delta\gamma^* = \gamma^*_{\mathrm{Au/STO}} - \gamma^*_{\mathrm{Co/STO}}$ and neglecting the slight differences in surface energies between the (1×2) and (2×2) reconstructed surfaces[45]. With $\gamma^*_{\mathrm{Co/STO}} = -1.18 \pm 0.3\,\mathrm{J/m^2}$ and $\gamma^*_{\mathrm{Au/STO}} = -0.45 \pm 0.09\,\mathrm{J/m^2}$, we compute $\gamma_{\mathrm{Co/Au}} > 0.73 \pm 0.39\,\mathrm{J/m^2}$. Note that these values indicate preferential binding of Co to STO, which explains the observed Co segregation to the substrate/nanowire interface. We also stress that the Au/STO interface used for calculation is of (111)//(001) and not of (001)//(001) type, as in our experiments. An alternative approach consists in relying only on DFT data. The aforementioned Co/STO adhesion work needs to be converted into an interface energy via $W^{\mathrm{adh}}_{\mathrm{Co/STO}} = \sum_{\mathrm{Co,STO}} E^{\mathrm{surf}} - \gamma_{\mathrm{Co/STO}}$. For consistency, we use the same literature references as those employed by Silly *et al.*[46, 47]: $E^{\mathrm{surf},(001)}_{\mathrm{Co}} = 2.78\mathrm{J/m^2}$ and $E^{\mathrm{surf},(001)}_{\mathrm{STO}} = 1.46\,\mathrm{J/m^2}$. With these values, we obtain

$\gamma_{\mathrm{Co/Au}} > 1.1 \pm 0.4\,\mathrm{J/m^2}$, if we estimate a ± 0.10 J/m^2 error associated with the surface and interface energies[44]. Our approach thus suggests a rather high Co/Au interface energy, which exceeds that of similar immiscible systems like Fe-Au [48] ($\gamma_{\mathrm{Fe/Au}} \simeq 0.57\,\mathrm{J/m^2}$). It would be highly interesting to compare these result with *ab-initio* calculations in order to obtain an estimation of the quality of our approximations. To our knowledge, such theoretical work is not available yet.

C. Magnetoelastic coupling

As already shown in a previous section, an effective uniaxial magnetic anisotropy can be derived from temperature dependent coercive field measurements. In sample S3, the Co part of the wire exhibits a high aspect ratio which gives rise to a large uniaxial magnetostatic anisotropy contribution: $K_{\mathrm{MS}} = \frac{\mu_0 M_s^2}{4}(1-3P) = 3.1 \cdot 10^5 \mathrm{J/m^3}$. Here, $P \simeq 0.18$ denotes the porosity, or filling ratio of the composite[18]. Surprisingly, the measured value K_{eff} exceeds the shape induced anisotropy contribution by more than 40%. Considering the cube on cube epitaxy of the buried magnetic Co fcc phase, no difference between IP and OP measurements should be seen. However, as already put forward, the Co lattice shows a pronounced tetragonalization with an average relative lattice parameter increase in OP direction $\langle \epsilon_{zz} \rangle \simeq 3.3\%$. This gives rise to important magnetoelastic contributions. The magnetostriction coefficient λ_{001} of pure fcc Co is positive [49]: $\lambda_{001} = 102 \cdot 10^{-6}$, suggesting that strain increases the anisotropy, as observed in our experiments. A quantitative approximation of the effect can be given as well. Based on the aforementioned magnetostriction value, we calculate an effective strain-induced anisotropy *via* $K_{\mathrm{ME}} = \frac{3}{2}\lambda_{001}\mu(\langle \epsilon_{zz} \rangle - \langle \epsilon_{rr} \rangle)$. With the room temperature Co fcc shear modulus[50] $\mu = 38\,\mathrm{GPa}$ and neglecting the average in-plane strain $\langle \epsilon_{rr} \rangle$, which is usually small in this type of vertical nanocomposite[17, 18, 21], we eventually obtain $K_{\mathrm{ME}} = 1.9 \cdot 10^5 \mathrm{J/m^3}$. This value is in reasonable agreement with $K_{\mathrm{eff}} - K_{\mathrm{MS}} = 1.3 \cdot 10^5 \mathrm{J/m^3}$. Axial strain resulting from vertical nanowire-matrix coupling thus provides a satisfactory explanation for the discrepancy between the measured anisotropy and shape induced contributions.

V. CONCLUSION

In this paper, we showed how sequential deposition of Au, Co and STO on $SrTiO_3$(001) substrates can be used to grow nanocolumnar composites consisting of bimetallic Co-Au wires, vertically embedded in a STO matrix. Our work allows to draw three main conclusions: *i)* in contrast to earlier studies on three phase nanocolumnar composites where CS structures were reported[19], the present results unveil bilayered segregation patterns, reminiscent of Janus-like phase separation, observed in rotationally symmetric nanoalloys. Comparing the free energy of such a segregation pattern with a CS configuration provides a lower bound for the Co/Au interface energy. We obtain $\gamma_{\mathrm{Co/Au}} > 0.73 \pm 0.39\,\mathrm{J/m^2}$, when relying on experimental data, while $\gamma_{\mathrm{Co/Au}} > 1.1 \pm 0.4\,\mathrm{J/m^2}$ is calculated when using exclusively simulation results. *ii)* The peculiar nanoarchitecture of the composite gives rise to highly anisotropic magnetic and optical properties, which can, in principle, be tuned by changing the growth parameters, *i.e.*, the nanowire diameter, the Co/Au concentration or the thin film thickness. *iii)* Vertical epitaxy not only provides control over the morphology of the composite, but allows to tune its crystallographic properties: the Co-rich phase is of fcc type. Epitaxial coupling to the matrix results in a rather pronounced tetragonalization which gives rise to large magnetoelastic effects.

Taken together, the present results highlight the versatility of vertical self-assembly, as a growth strategy to obtain multiphased epitaxial nanocolumnar structures, and pave the way for the development of a new class of thin films, which hold promise as a platform for future magnetoplasmonic studies.

VI. ACKNOWLEDGEMENTS

The authors thank the SOLEIL staff for smoothly running the facility, J.-M. Guigner (IMPMC) for access to the TEM facilities and the staff of the MPBT platform of Sorbonne Université for their support. The STEM studies were carried out on a microscope acquired as part of the TEMPOS project (ANR-10-EQPX-0050). This work was supported by French state funds managed by the ANR within the "Investissements d'Avenir" (ANR-11-IDEX-0004-02) within the framework of the Cluster of Excellence MATISSE. M. Hennes acknowledges financial support from the French Embassy in Berlin and Campus France.

[1] T. B. Massalki, H. Okamoto, and P. R. Subramanian, eds., *Binary Alloy Phase Diagrams*, 2nd ed. (ASM International: Metals Park, 1990).

[2] J.-P. Palomares-Baez, E. Panizon, and R. Ferrando, Nano Lett. **17**, 5394 (2017).

[3] K. Yang, C. Clavero, J. R. Skuza, M. Varela, and R. A. Lukaszew, J. Appl. Phys **107**, 103924 (2010).

[4] A. Gaspar, C. Alfonso, G. Antonio, and G. M. Uju, Adv. Opt. Mater **1**, 10 (2013).

[5] D. Martin-Becerra, J. M. Garcia-Martín, Y. Huttel, and G. Armelles, J. Appl. Phys **117**, 053101 (2015).

[6] P. Kluth, B. Hoy, B. Johannessen, S. G. Dunn, G. J. Foran, and M. C. Ridgway, Appl. Phys. Lett **89**, 153118 (2006).

[7] Y. Xu and J. Wang, Advanced Materials **20**, 994 (2006).

[8] V. Dupuis, G. Khadra, A. Hillion, A. Tamion, J. Tuaillon-Combes, L. Bardotti, and F. Tournus, Phys. Chem. Chem. Phys. **17**, 27996 (2015).

[9] B. Jang, E. Pellicer, M. Guerrero, X. Chen, H. Choi, B. J. Nelson, J. Sort, and S. Pan, ACS Appl. Mater. Interfaces **6**, 14583 (2014).

[10] L. Mohaddes-Ardabili, H. Zheng, S. B. Ogale, B. Hannoyer, W. Tian, J. Wang, S. E. Lofland, S. R. Shinde, T. Zhao, Y. Jia, L. Salamanca-Riba, D. G. Schlom, M. Wuttig, and R. Ramesh, Nat. Mater **3**, 533 EP (2004).

[11] F. Vidal, Y. Zheng, J. Milano, D. Demaille, P. Schio, E. Fonda, and B. Vodungbo, Appl. Phys. Lett. **95**, 152510 (2009).

[12] F. Vidal, Y. Zheng, P. Schio, F. J. Bonilla, M. Barturen, J. Milano, D. Demaille, E. Fonda, A. J. A. de Oliveira, and V. H. Etgens, Phys. Rev. Lett. **109**, 117205 (2012).

[13] S. Kawasaki, R. Takahashi, T. Yamamoto, M. Kobayashi, H. Kumigashira, J. Yoshinobu, F. Komori, A. Kudo, and M. Lippmaa, Nature Commun. **7**, 11818 (2016).

[14] L. Li, L. Sun, J. S. Gomez-Diaz, N. L. Hogan, P. Lu, F. Khatkhatay, W. Zhang, J. Jian, J. Huang, Q. Su, M. Fan, C. Jacob, J. Li, X. Zhang, Q. Jia, M. Sheldon, A. Al, X. Li, and H. Wang, Nano Lett. **16**, 3936 (2016).

[15] J. Huang, L. Li, P. Lu, Z. Qi, X. Sun, X. Zhang, and H. Wang, Nanoscale **9**, 7970 (2017).

[16] M. Hennes, V. Schuler, X. Weng, J. Buchwald, D. Demaille, Y. Zheng, and F. Vidal, Nanoscale **10**, 7666 (2018).

[17] F. J. Bonilla, A. Novikova, F. Vidal, Y. Zheng, E. Fonda, D. Demaille, V. Schuler, A. Coati, A. Vlad, Y. Garreau, M. Sauvage Simkin, Y. Dumont, S. Hidki, and V. Etgens, ACS Nano **7**, 4022 (2013).

[18] V. Schuler, J. Milano, A. Coati, A. Vlad, M. Sauvage-Simkin, Y. Garreau, D. Demaille, S. Hidki, A. Novikova, E. Fonda, Y. Zheng, and F. Vidal, Nanotechnology **27**, 495601 (2016).

[19] D. H. Kim, X. Y. Sun, N. M. Aimon, J. J. Kim, M. J. Campion, H. L. Tuller, L. Kornblum, F. J. Walker, C. H. Ahn, and C. A. Ross, Adv. Funct. Mater **25**, 3091 (2015).

[20] T. Ohnishi, K. Shibuya, T. Yamamoto, and M. Lippmaa, J. Appl. Phys. **103**, 103703 (2008).

[21] V. Schuler, F. J. Bonilla, D. Demaille, A. Coati, A. Vlad, Y. Garreau, M. Sauvage-Simkin, A. Novikova, E. Fonda, S. Hidki, V. Etgens, F. Vidal, and Y. Zheng, Nano Res. **8**, 1964 (2015).

[22] X. Weng, M. Hennes, A. Coati, A. Vlad, Y. Garreau, M. Sauvage-Simkin, E. Fonda, G. Patriarche, D. Demaille, F. Vidal, and Y. Zheng, Phys. Rev. Materials **2**, 106003 (2018).

[23] B. Ravel and M. Newville, J. Synchrotron Radiat. **12**, 537 (2005).

[24] The reference spectrum taken from [25] has been shifted for Co K-edge energy alignement.

[25] G. Zhang, Z. Y. Wu, A. Li, Y. Wang, J. Zhang, M. I. Abbas, R. Hu, X. Ni, Y. Tong, and Y. Hwu, Phys. Rev. B **69**, 115405 (2004).

[26] C. Granqvist and O. Hunderi, Phys. Rev. B **16**, 3513 (1977).

[27] M. P. Sharrock, J. Appl. Phys. **76**, 6413 (1994).

[28] I. Mouton, E. Talbot, C. Pareige, R. Lardé, and D. Blavette, J. Appl. Phys. **115**, 053515 (2014).

[29] L. E. Marbella, C. M. Andolina, A. M. Smith, M. J. Hartmann, A. C. Dewar, K. A. Johnston, O. H. Daly, and J. E. Millstone, Adv. Funct. Mater. **24**, 6532 (2014).

[30] F. Calvo, ed., *Nanoalloys* (Elsevier, Oxford, 2013).

[31] R. Ferrando, J. Jellinek, and R. L. Johnston, Chemical Reviews **108**, 845 (2008).

[32] A. A. Dzhurakhalov and M. Hou, Phys. Rev. B **76**, 045429 (2007).

[33] Y. Wang and M. Hou, J. Phys. Chem. C **116**, 10814 (2012).

[34] R. Ferrando, J. Phys.: Condens. Matter (2015).

[35] M. Hennes, J. Buchwald, U. Ross, A. Lotnyk, and S. G. Mayr, Phys. Rev. B **91**, 245401 (2015).

[36] F. Calvo, Phys. Chem. Chem. Phys. **17**, 27922 (2015).

[37] D. Bochicchio and R. Ferrando, Phys. Rev. B **87**, 165435 (2013).

[38] E. Maras, F. Berthier, and B. Legrand, J. Phys. Chem. C **120**, 22670 (2016).

[39] D. Bochicchio, R. Ferrando, E. Panizon, and G. Rossi, Journal of Physics: Condensed Matter **28**, 064005 (2016).

[40] W. Tyson and W. Miller, Surf. Sci. **62**, 267 (1977).

[41] F. Silly and M. R. Castell, Appl. Phys. Lett **87**, 053106 (2005).

[42] I. I. Oleinik, E. Y. Tsymbal, and D. G. Pettifor, Phys. Rev. B **65**, 020401 (2001).

[43] K. Zhao, D. Chen, and D. Li, Comput. Mater. Sci. **50**, 98 (2010).

[44] F. Silly and M. R. Castell, Phys. Rev. Lett. **96**, 086104 (2006).

[45] O. Warschkow, M. Asta, N. Erdman, K. R. Poeppelmeier, D. E. Ellis, and L. D. Marks, Surf. Sci. **573**, 446 (2004).

[46] M. Alde'n, S. Mirbt, H. L. Skriver, N. M. Rosengaard, and B. Johansson, Phys. Rev. B **46**, 6303 (1992).

[47] K. Johnston, M. R. Castell, A. T. Paxton, and M. W. Finnis, Phys. Rev. B **70**, 085415 (2004).

[48] M. Benoit, C. Langlois, N. Combe, H. Tang, and M.-J. Casanove, Phys. Rev. B **86**, 075460 (2012).

[49] R. Wu, L. Chen, and A. Freeman, J. Magn. Magn. Mater **170**, 103 (1997).

[50] H. J. Leamy and H. Warlimont, Phys. Status Solidi (b) **37**, 523 (1970).